Electronic Supplementary Material

$ZnGeSe_2$ Monolayer: Water-Splitting Photocatalyst with Ultrahigh Solar Conversion Efficiency

Guoting Nan[1, 2], Wei Zhang[1, 2], Xiaojun Yan[1,2], Xi Qin[1], Song Wu[1], Rufei Tang[3], Ming-Xia Tang[3], Lei Hu*[1], Lili Liu[3], Shifa Wang[1], Yuming Feng*[1, 2], Wencai Yi*[4]

1. College of Electronic and Information Engineer, Chongqing Three Gorges University, Chongqing, 404100, China

2. College of Computer Science and Engineering, Chongqing Three Gorges University, Chongqing, 404100, China

3. College of Teacher Education, Chongqing Three Gorges University, Chongqing, 404100, China

4. Laboratory of High-Pressure Physics and Material Science (HPPMS), Advanced Research Institute of Multidisciplinary Science, Qufu Normal University, Qufu, Shandong, 273165, China

Corresponding Author

Lei Hu: huleisanxu@163.com

Yuming Feng: ymfeng@sanxiau.edu.cn

Wencai Yi: yiwc@qfnu.edu.cn

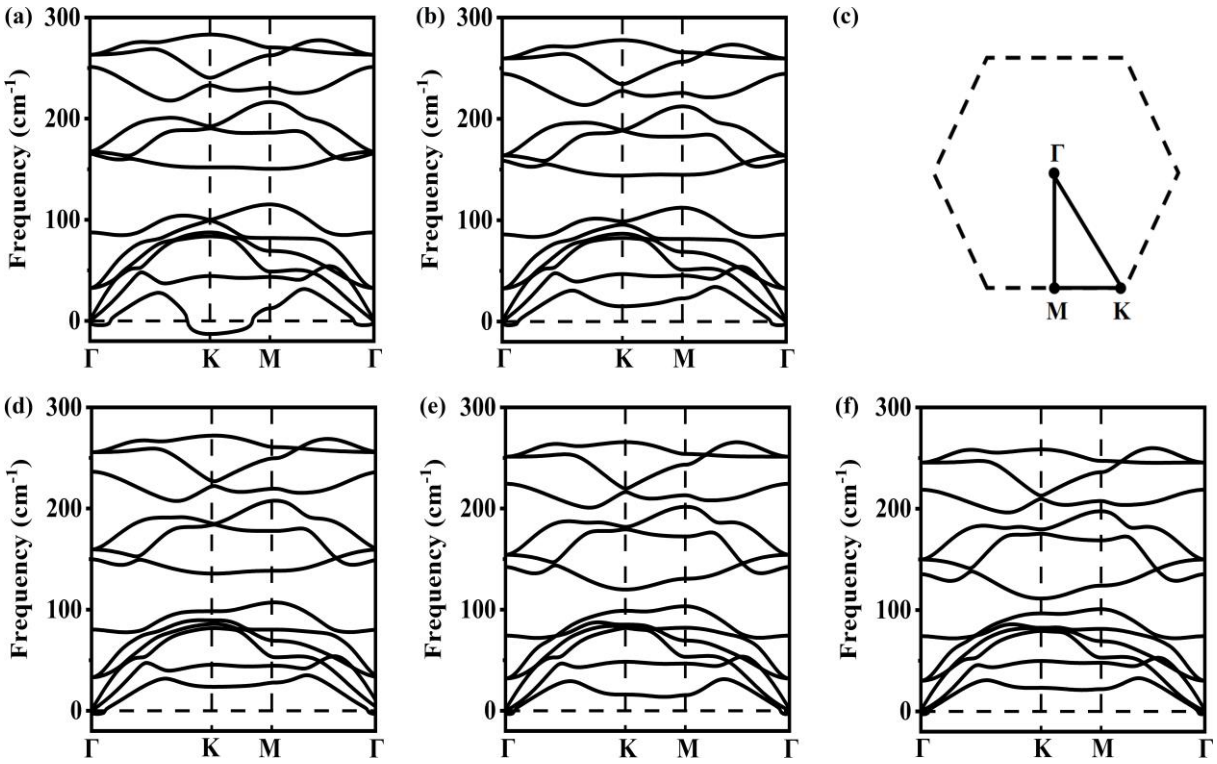

Figure S1. The phonon spectrum curves of the $ZnGeSe_2$ monolayer under the biaxial strains of (a) -2%, (b) -1%, (d) 0%, (e) +1%, and (f) +2%; (c) The high symmetry *k*-points along the first Brillouin Zone

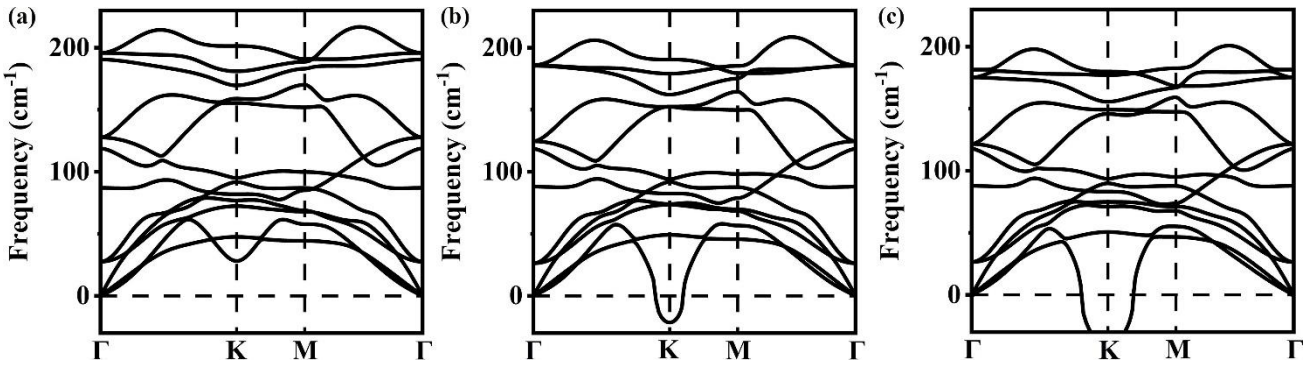

Figure S2. The phonon spectrum of single-layer $ZnGeSe_2$ at the tensile biaxial strain of (a) 11%, (b)12%, and (c) 13%

Single-layer $ZnGeSe_2$ exhibits no imaginary frequencies at the biaxial strain of 11% (Figure S2a). Imaginary frequencies appear at the biaxial strain of 12% (Figure S2b), and becomes more significant at the biaxial strain of 13% (Figure S2c). Hence, single-layer $ZnGeSe_2$ gets dynamically unstable when exposed to the 12% biaxial strain.

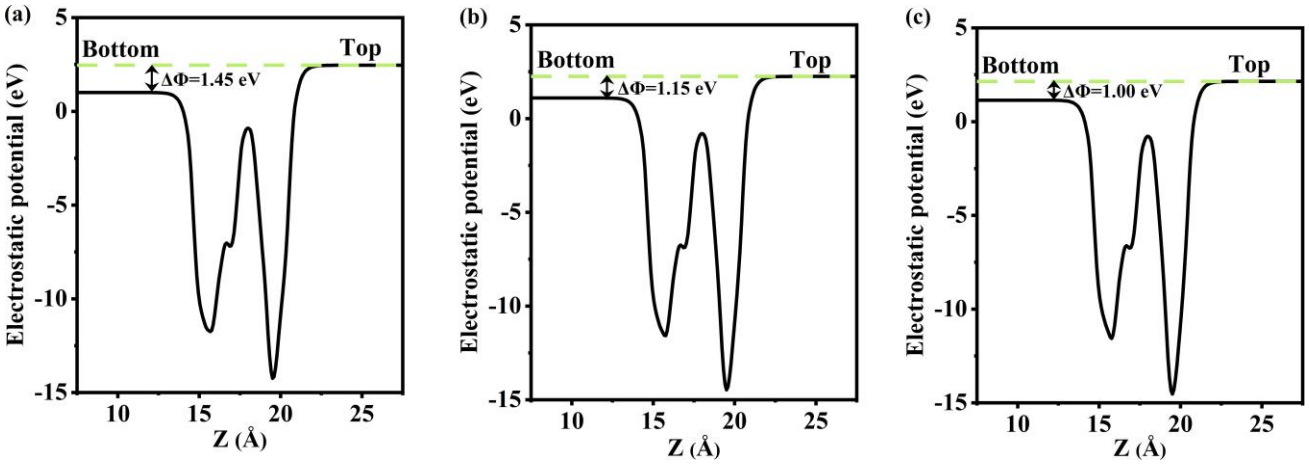

Figure S3. The planar average potential along the *z* direction of the $ZnGeSe_2$ monolayer under the biaxial strain of (a) -1%, (b) +1%, and (c) +2%

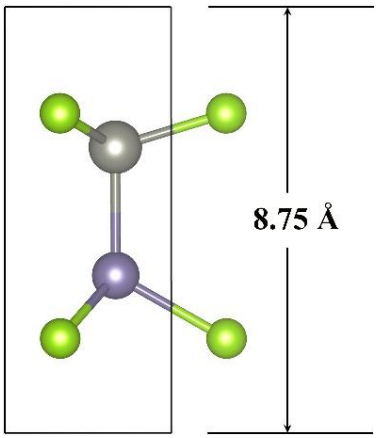

Figure S4. The bulk $ZnGeSe_2$ crystal containing one unit

For the calculation of the effective thickness for the $ZnGeSe_2$ monolayer, a bulk crystal containing one $ZnGeSe_2$ unit is built. The lattice constant of bulk $ZnGeSe_2$ along the vertical direction is 8.75 Å, and it is considered as the effective thickness of the $ZnGeSe_2$ monolayer.

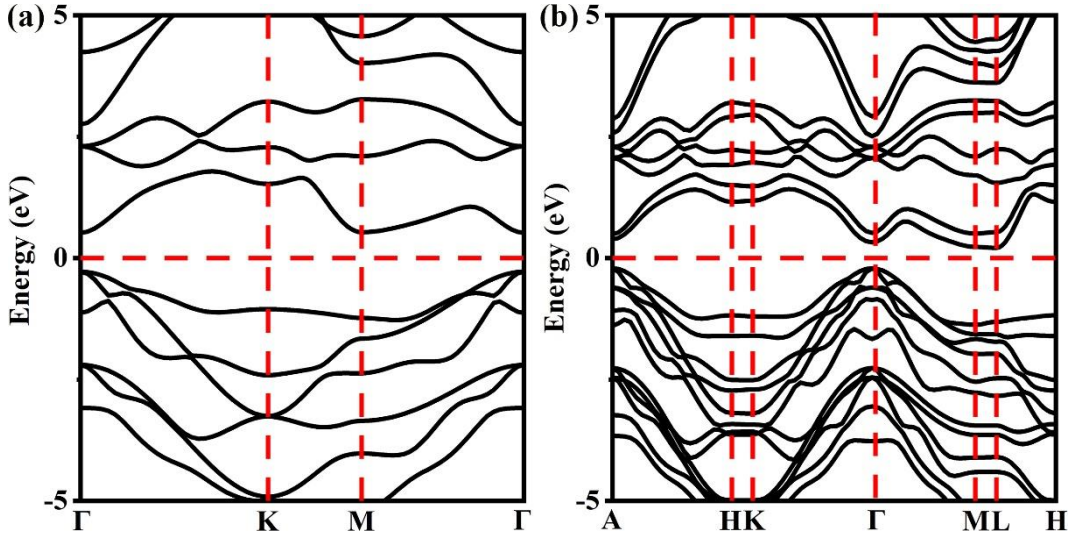

Figure S5. The bandgap of (a) single-layer and (b) bulk $ZnGeSe_2$ at the PBE level

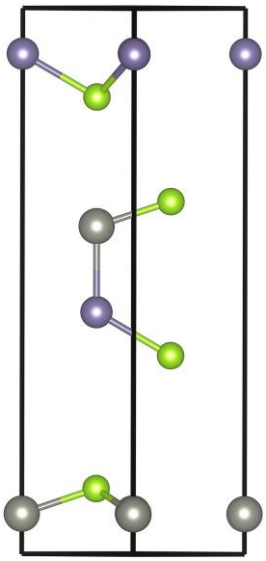

Figure S6. The schematics of the assumed bulk $ZnGeSe_2$ similar to bulk GaSe

Single-layer $ZnGeSe_2$ has no bulk forms at the present stage. Considering the structural similarity between single-layer $ZnGeSe_2$ (Se-Zn-Ge-Se) [1] and GaSe (Se-Ga-Se-Se)[2], we assume a bulk $ZnGeSe_2$ crystal containing two $ZnGeSe_2$ layers (Figure S6). At the PBE level, single-layer $ZnGeSe_2$ has a direct band gap of 0.80 eV (Figure S5a). From single-layer to bulk, a direct-to-indirect bandgap transition is observed. Obviously, the bandgap of bulk $ZnGeSe_2$ is reduced to 0.42 eV (Figure S5b). Bulk $ZnGeSe_2$ displays an indirect bandgap from the Γ to L points. We do not study the photocatalytic property of bulk $ZnGeSe_2$ because of its possible high recombination rates as usual bulk crystals [3].

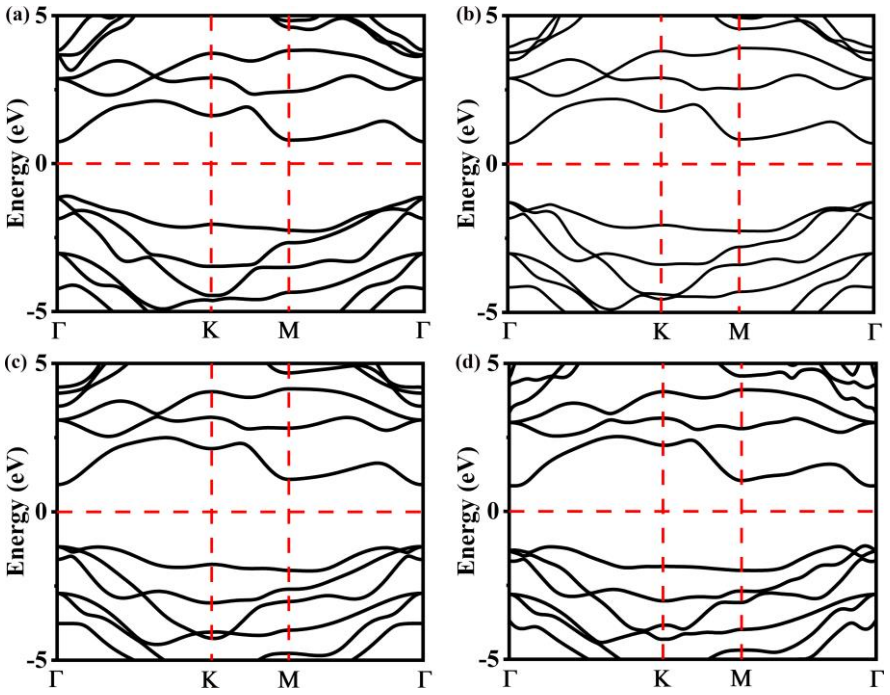

Figure S7. The calculated band structures of the $ZnGeSe_2$ monolayer under the biaxial strain of (a) -1%, (b) 0%, (c) +1%, and (d) +2% by G_0W_0+Wannier

The $ZnGeSe_2$ monolayer shows direct or quasi-direct bandgaps at the Gamma point by G_0W_0, and the bandgaps at the Gamma point are 1.88, 1.99, 2.10 and 2.18 eV under -1%, 0%, +1%, and +2% biaxial strain, respectively.

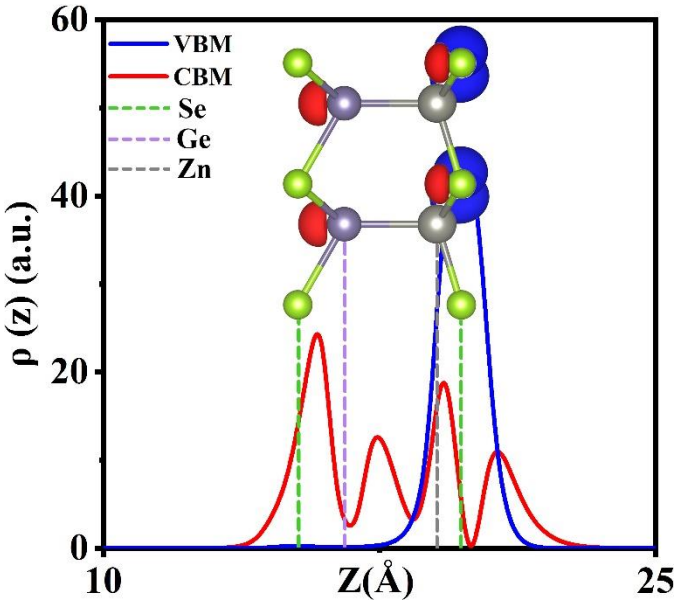

Figure S8. The partial charge density distribution of CBM (red) and VBM (blue) aligned with the plane-integrated electron density (ρ) along the *z*-direction of the $ZnGeSe_2$ monolayer without strain;

Note the isosurface value is set as 0.025 e·Å^{-3}.

For direct comparison, the partial charge density of CBM and VBM has been aligned with the plane-integrated electron density (ρ) along the *z*-direction. As shown in Figure S8, the maximum charge density of CBM is located between the selenium (Se) and germanium (Ge) atomic layers, and the VBM charge density is mainly located around the top Se atomic layer.

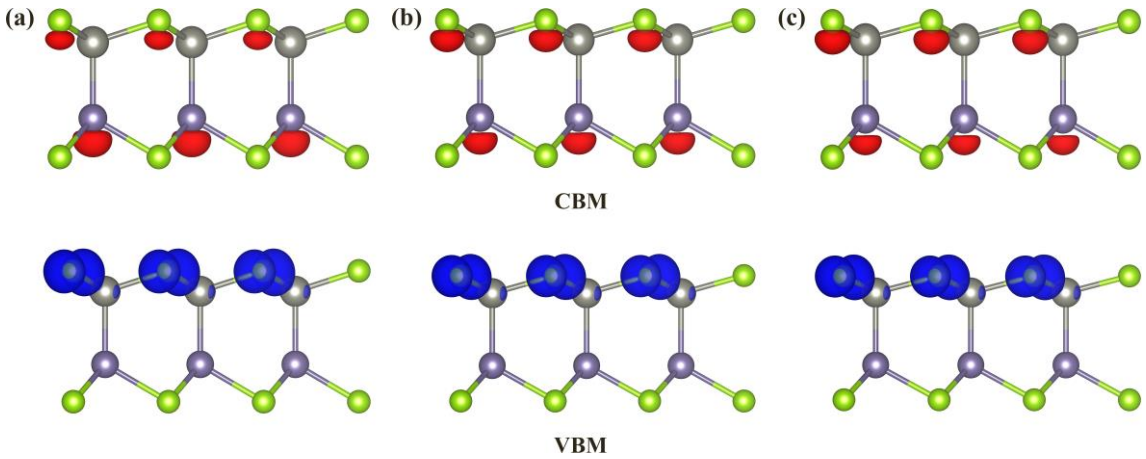

Figure S9. The partial charge density distribution of CBM (red) and VBM (blue) with an isosurface value of 0.025 e·Å of the $ZnGeSe_2$ monolayer under the biaxial strain of (a) -1%, (b) +1%, and (c) +2%

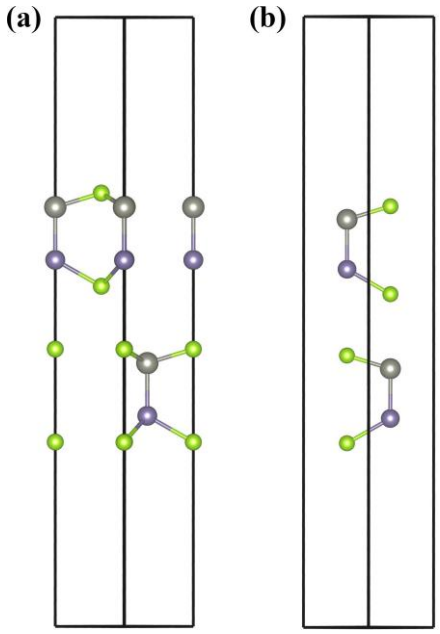

Figure S10. The schematics of bilayer AA and AB $ZnGeSe_2$

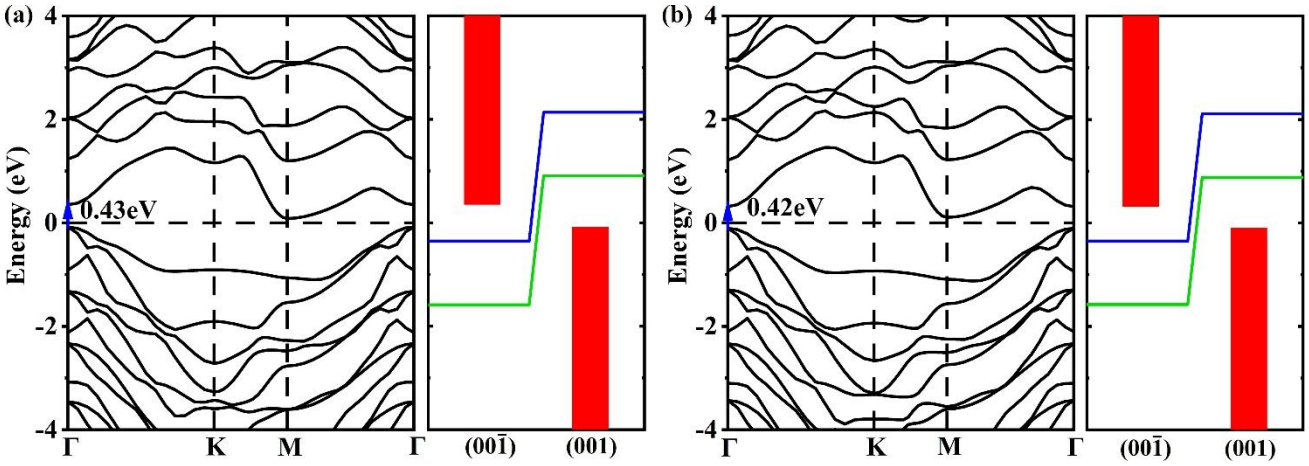

Figure S11. The band structure (Left) and water-splitting property (Right) of (a) AA and (b) AB bilayers at the HSE06 level. The upper and lower red columns denote the CBM and the VBM, respectively. The blue and green lines represent the redox potentials of H^+/H_2 and H_2O/O_2, respectively.

Considering the structure similarity between single-layer $ZnGeSe_2$ [1] and GaSe [2], bilayer AA and AB $ZnGeSe_2$ (Figure S10) are constructed. As shown in **Table S1**, the in-plane constants (3.92 Å) of bilayer AA and AB are not modified in comparison with that of single-layer $ZnGeSe_2$. The effective heights *h* of bilayer AA and AB are considered as the twice of that of single-layer $ZnGeSe_2$. The intrinsic dipole moments μ (0.65 Debye) of AA and AB are also twice that of single-layer $ZnGeSe_2$ (0.32 Debye).

The bandgaps of bilayer AA (0.43 eV) and AB (0.42 eV) are much-decreased, in comparison with that (1.37 eV) of single-layer $ZnGeSe_2$. As shown in Figure S11, bilayer AA and AB hold suitable band edges for solar water-splitting.

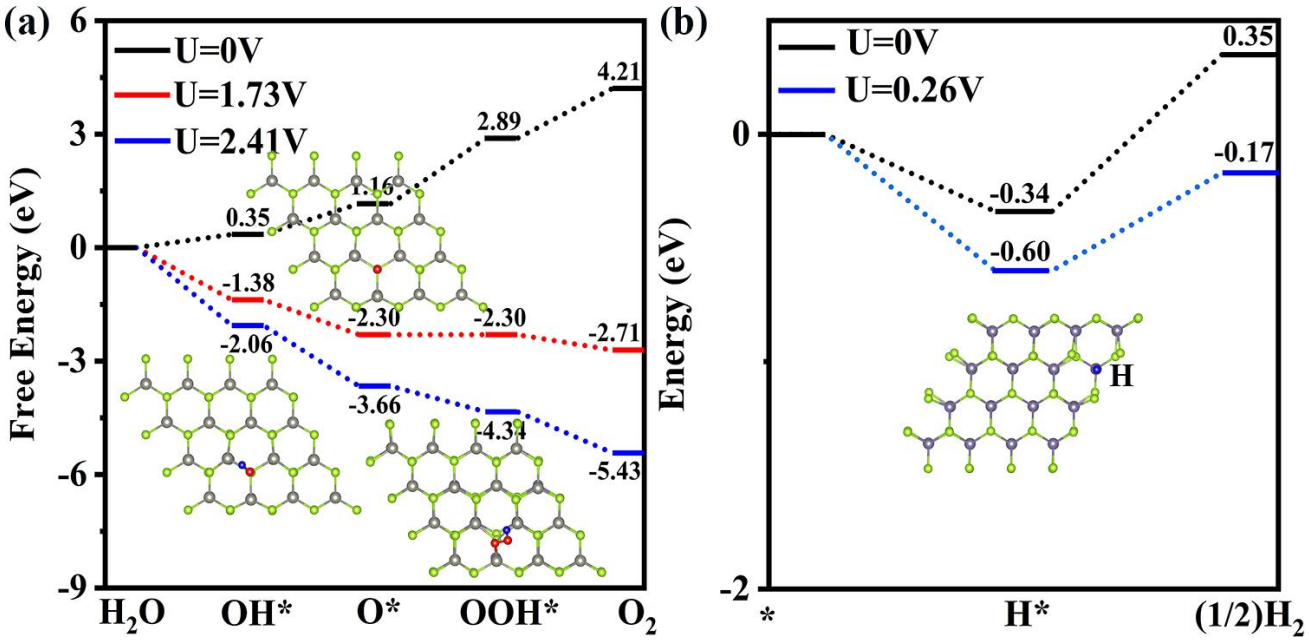

Figure S12. (a) The Gibbs free energy change of OER on the upper Se atomic layer; (b) The Gibbs free energy of HER at pH=3 on the Ge atomic layer of the $ZnGeSe_2$ monolayer under zero strain

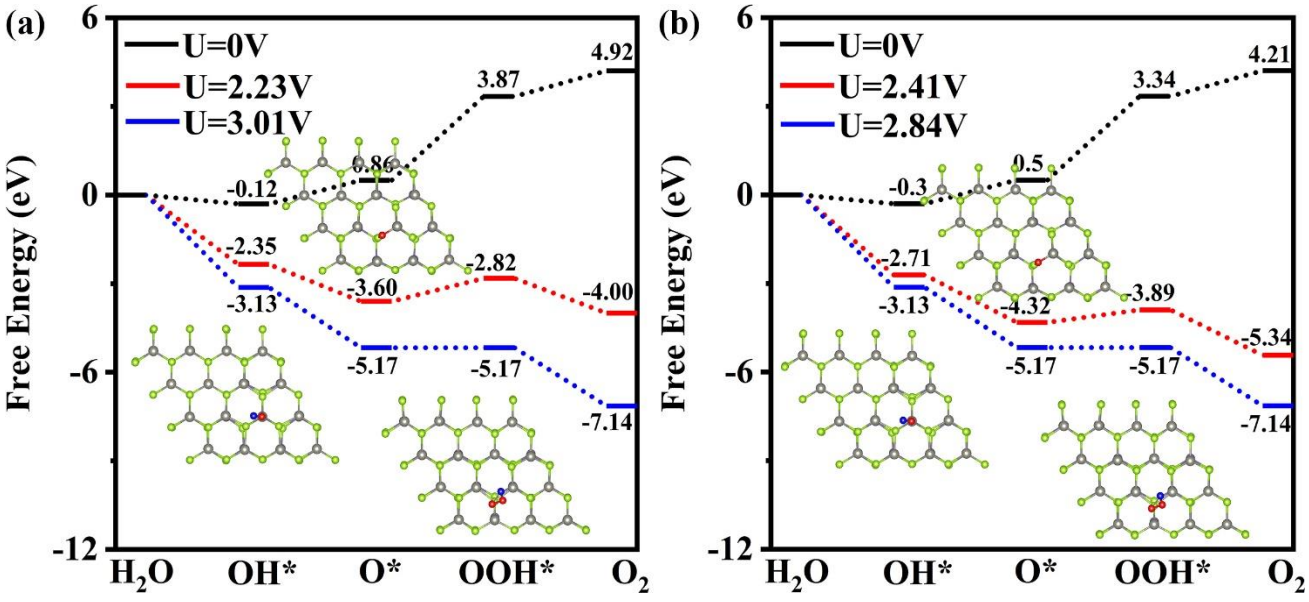

Figure S13. Another feasible OER route at (a) pH=0 and (b) pH=3

As shown in previous calculations [4], the OH, O, and OOH locations in the OH*, O*, and OOH* intermediates approach each other. Hence, we first find out the location of the O atom in the O* intermediate, by considering four possible configurations including the O atom on the top of the Se atom, the Zn atom, the Zn-Se bond, and the hexagonal ring on the (001) surface of the $ZnGeSe_2$

monolayer. We find the most stable configuration is the configuration of O on the Zn-Se bond. On the basis of the O* intermediate, we obtain the most stable configurations of the OH* and OOH* intermediates (Figure S13).

The limiting step is third step with a Gibbs free energy change of 3.01 eV at pH=0 (Figure S13a). Under the external potential of 2.23 eV (Table 1 in the main manuscript) provided by photogenerated holes, the OER barrier becomes 0.78 eV. On the other hand, the exothermic effect (1.25 eV) is apparently stronger than the endothermic effect (0.78 eV). Hence, the OER based on this reaction route is also feasible. Under the condition of pH=3 (Figure S13b), at the external potential of 2.41 provided by photogenerated holes (Table 1 in the main manuscript), the exothermic effect (1.61eV) is also stronger than the endothermic effect (0.43 eV), indicating a smooth OER process.

Moreover, we ascertain the location of the H atom in the H* intermediate, by considering four possible configurations including H on the top Se atom, the Ge atom, the Ge-Se bond, and the hexagonal ring of on the $(00\bar{1})$ surface the $ZnGeSe_2$ monolayer. We find the most stable configuration is on the configuration of H on the Ge atom, which is the research target in our main manuscript.

ESM-1. Computational Details for G_0W_0+BSE

(1) For the optical absorption calculations, the 8×8×1 *k*-point grid is sampled in the G_0W_0+BSE calculations[5-8]. (1) GGA-PBE calculations with an energy convergence criterion of 1×10^{-8} eV are performed; (2) GGA-PBE calculations are restarted to allow full optical transitions, where 240 electronic bands are included; (3) G_0W_0 calculations are carried out to obtain quasi-particle excitations, where an energy cutoff of 150 eV for the response functions, the spectral method and 72 frequency points are adopted; (4) The Bethe–Salpeter equation is solved, with 19 highest valence bands and 19 lowest unoccupied conduction bands included.

ESM-2. Calculation of the Gibbs free energy for the OER and HER

The four-step OER processes are listed by using the following formula [9]:

$$* + H_2O \rightarrow OH^* + H^+ + e^-$$

$$OH^* \rightarrow O^* + H^+ + e^-$$

$$O^* + H_2O \rightarrow OOH^* + H^+ + e^-$$

$$OOH^* \rightarrow * + O_2 + H^+ + e^-$$

where $*$ indicates the adsorbed material ($ZnGeSe_2$ monolayer), OH^*, O^* and OOH^* represent the intermediates. For all the calculations, spin-polarization is taken into account. By considering the zero-point energy and entropy corrections [10], the expression of ΔG can be written as $\Delta G = \Delta E_{ads} + \Delta E_{ZPE} - T\Delta S$, where ΔE_{ads} is the adsorption energy, ΔE_{ZPE} and ΔS are the difference of zero point energy and entropy difference between the adsorbed state and the gas phase, respectively. *T* represents the room temperature of 300 *K*.

For each reaction of oxidation generation, ΔG can be written as [4]:

$$\Delta G_1 = G_{OH^*} + \frac{1}{2}G_{H_2} - G^* - G_{H_2O} + \Delta G_U - \Delta G_{pH} \qquad Eq.\ (S1)$$

$$\Delta G_2 = G_{O^*} + \frac{1}{2}G_{H_2} - G_{OH^*} + \Delta G_U - \Delta G_{pH} \qquad Eq.\ (S2)$$

$$\Delta G_3 = G_{OOH^*} + \frac{1}{2}G_{H_2} - G_{O^*} - G_{H_2O} + \Delta G_U - \Delta G_{pH} \qquad Eq.\ (S3)$$

$$\Delta G_4 = G^* + \frac{1}{2}G_{H_2} + G_{O_2} - G_{OOH^*} + \Delta G_U - \Delta G_{pH} \qquad Eq.\ (S4)$$

Where ΔG_U ($\Delta G_U = -eU$) denotes extra potential bias provided by an electron in the electrode, and U is the electrode potential relative to the standard hydrogen electrode (SHE). ΔG_{pH} ($\Delta G_{pH} = k_B T \times ln10 \times pH$) represents the free energy contributed in different pH.

Moreover, the hydrogen evolution reaction can be decomposed into two steps:

$$* + H^+ + e^- \rightarrow H^*$$

$$H^* + H^+ + e^- \rightarrow * + H_2$$

ESM-3. The VASP CONTCAR file of the $ZnGeSe_2$ monolayer under zero strain

$ZnGeSe_2$

1.00000000000000

3.3959177702111485 -1.9606340387772390 0.0000000000000000

0.0000000000000000 3.9212680775544797 0.0000000000000000

0.0000000000000000 0.0000000000000000 35.0000000000000000

Zn Ge Se

1 1 2

Direct

0.3333299999999966 0.6666700000000034 0.5456436392416210

0.3333299999999966 0.6666700000000034 0.4712509147795727

0.6666700000000034 0.3333300000000037 0.5651448186706348

0.6666700000000034 0.3333300000000037 0.4339806273081692

ESM-4. Band Alignment Method

For solar water splitting, the basic requirement is that the CBM level relative to the vacuum level is higher than the H^+/H_2 reduction potential (E_{H^+/H_2}), while the VBM level relative the vacuum level is lower than the H_2O/O_2 oxidation potential (E_{H_2O/O_2}). Hence, the following equations are obtained.

$$E'_{\mathrm{CBM}} - E_{\mathrm{Vacuum}} > E_{H^+/H_2} \qquad Eq.\ (S5)$$

$$E'_{\mathrm{VBM}} - E_{\mathrm{Vacuum}} < E_{H_2O/O_2} \qquad Eq.\ (S6)$$

$$E'_{\mathrm{CBM}} > E_{\mathrm{Vacuum}} + E_{H^+/H_2} \qquad Eq.\ (S7)$$

$$E'_{\mathrm{VBM}} < E_{\mathrm{Vacuum}} + E_{H_2O/O_2} \qquad Eq.\ (S8)$$

Where E'_{CBM} and E'_{VBM} are the VBM and VBM levels directly extracted from the VASP band structure, with the fermi level not reset. The E_{H^+/H_2} and E_{H_2O/O_2} values are -4.44 and -5.67 eV, respectively.

Typically, the band structure is displayed with the Fermi level being reset as zero. Thus, the following equations are obtained.

$$E'_{\mathrm{CBM}} - E_{\mathrm{fermi}} > E_{\mathrm{Vacuum}} + E_{H^+/H_2} - E_{fermi} \qquad Eq.\ (S9)$$

$$E'_{\mathrm{VBM}} - E_{\mathrm{fermi}} < E_{\mathrm{Vacuum}} + E_{H_2O/O_2} - E_{fermi} \qquad Eq.\ (S10)$$

For simplicity:

$$E_{CBM} = E'_{\mathrm{CBM}} - E_{\mathrm{fermi}} \qquad Eq.\ (S11)$$

$$E_{VBM} = E'_{\mathrm{VBM}} - E_{\mathrm{fermi}} \qquad Eq.\ (S12)$$

$$E'_{H^+/H_2} = E_{\mathrm{Vacuum}} + E_{H^+/H_2} - E_{fermi} \qquad Eq.\ (S13)$$

$$E'_{H_2O/O_2} = E_{\mathrm{Vacuum}} + E_{H_2O/O_2} - E_{fermi} \qquad Eq.\ (S14)$$

We obtain the following equations. The solar water-splitting requirement can be straightly written as:

$$E_{CBM} > E'_{H^+/H_2} \qquad Eq.\ (S15)$$

$$E_{VBM} < E'_{H_2O/O_2} \qquad Eq.\ (S16)$$

Now, the E_{CBM} and E_{VBM} are the CBM and VBM levels extracted from the band structures with Fermi level being set as the zero level.

Due to the intrinsic dipole, single-layer $ZnGeSe_2$ has two vacuum levels. Thus, the following equations are obtained.

$$E^{bottom\prime}_{H^+/H_2} = E^{bottom}_{Vacuum} + E_{H^+/H_2} - E_{fermi} \qquad Eq.\ (S17)$$

$$E_{H_2O/O_2}^{bottom\prime} = E_{Vacuum}^{bottom} + E_{H_2O/O_2} - E_{fermi} \qquad Eq.\ (S18)$$

$$E_{H^+/H_2}^{top\prime} = E_{Vacuum}^{top} + E_{H^+/H_2} - E_{fermi} \qquad Eq.\ (S19)$$

$$E_{H_2O/O_2}^{top\prime} = E_{Vacuum}^{top} + E_{H_2O/O_2} - E_{fermi} \qquad Eq.\ (S20)$$

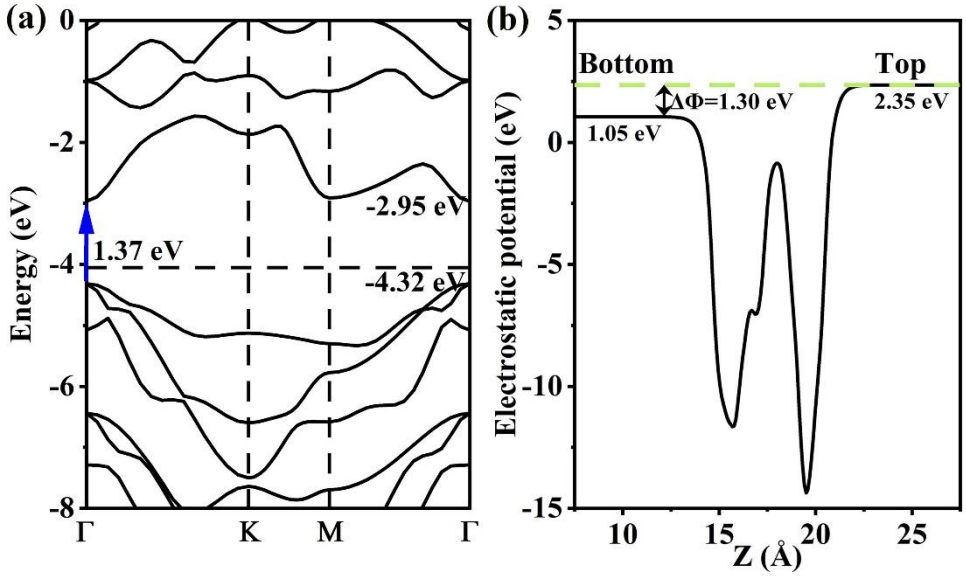

Figure S14. (a) The band structure and (b) the vacuum level of single-layer $ZnGeSe_2$ with the Fermi level not reset to the zero level.

The $ZnGeSe_2$ monolayer under zero strain is take as an example. From Figure S14, we obtain E_{Vacuum}^{bottom}=1.05 eV, E_{Vacuum}^{top}=2.35 eV, E'_{CBM}=-2.95 eV, and E'_{VBM}=-4.32 eV. The fermi level is -4.05 eV, i.e. E_{fermi} =-4.05 eV

$$E_{H^+/H_2}^{bottom\prime} = E_{Vacuum}^{bottom} + E_{H^+/H_2} - E_{fermi}\text{=1.05-4.44+4.05 =0.66 eV}$$

$$E_{H_2O/O_2}^{bottom\prime} = E_{Vacuum}^{bottom} + E_{H_2O/O_2} - E_{fermi}\text{=1.05-5.67+4.05 = -0.57 eV}$$

$$E_{H^+/H_2}^{top\prime} = E_{Vacuum}^{top} + E_{H^+/H_2} - E_{fermi}\text{=2.35-4.44+4.05 =1.96 eV}$$

$$E_{H_2O/O_2}^{top\prime} = E_{Vacuum}^{top} + E_{H_2O/O_2} - E_{fermi}\text{=2.35-5.67+4.05 =0.73 eV}$$

$$E_{CBM} = E'_{\mathrm{CBM}} - E_{\mathrm{fermi}}\text{= -2.95+4.05 =1.10 eV}$$

$$E_{VBM} = E'_{\mathrm{VBM}} - E_{\mathrm{fermi}}\text{= -4.32+4.05 = -0.27 eV}$$

Considering the VBM charge is distributed on the top (001) surface and the CBM is on the $(00\bar{1})$ surface, the requirement for solar water-splitting becomes:

$$E_{CBM} > E_{H^+/H_2}^{bottom\prime} \quad (1.10\ \text{eV} > 0.66\ \text{eV})$$

$$E_{VBM} < E_{H_2O/O_2}^{top\prime} \quad (-0.27\ \text{eV} < 0.73\ \text{eV})$$

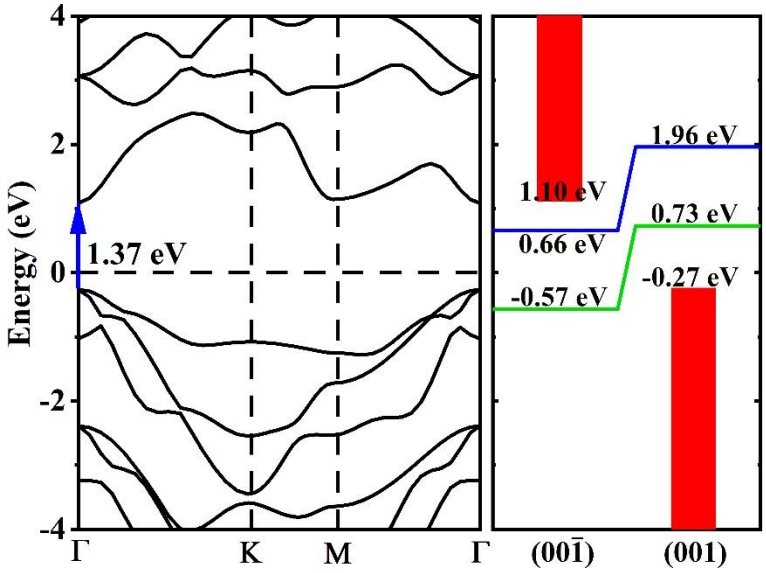

Figure S15. The band structure (Left) and water-splitting property (Right) of the $ZnGeSe_2$ monolayer under zero strain at the HSE06 level. The upper and lower red columns denote the CBM and the VBM, respectively. The blue and green lines represent the redox potentials of H^+/H_2 and H_2O/O_2, respectively

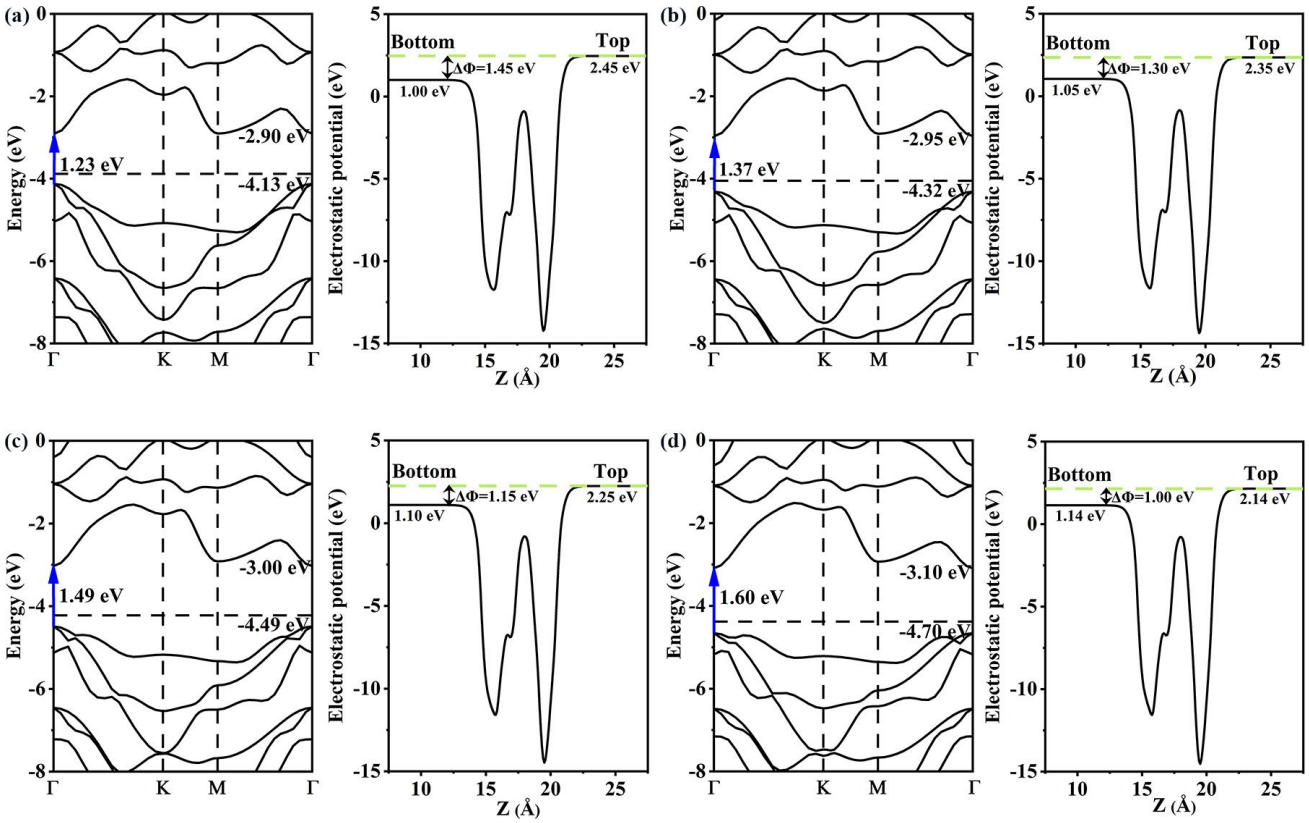

Figure S16. The band structure and the vacuum level of the $ZnGeSe_2$ monolayer under the (a) -1%, (b) 0%, (c) +1%, and +2% biaxial strain with the Fermi level not reset to the zero level. The Fermi levels are -3.88, -4.05, -4.21 and -4.37 eV, respectively.

Table S1. The calculated elastic constants ($N \cdot m^{-1}$) of the $ZnGeSe_2$ monolayer under biaxial strain

System	C_{11}	C_{12}	C_{66}
-1%	57.01	21.49	17.76
0%	55.93	21.59	17.15
+1%	55.16	22.15	16.52
+2%	54.11	22.42	15.84

Table S2. The in-plane lattice constants *a* (Å), effective thickness *h* (Å), intrinsic dipole moment μ (Debye), electrostatic potential in the vacuum region $\Delta\Phi$(eV), Φ_h(eV) and Φ_l (eV) of AA and AB bilayer $ZnGeSe_2$.

Materials	*a* (Å)	*h* (Å)	μ (Debye)	$\Delta\Phi$ (eV)	Φ_h (eV)	Φ_l(eV)
AA	3.92	17.5	0.65	1.75	4.83	3.08
AB	3.92	17.5	0.65	1.73	4.56	2.83

Table S3. The DFT energy *E* (eV), the zero-point energy correction E_{ZPE} (eV), the entropy contribution *TS* at 300 K (eV), and the Gibbs free energy *G* (eV)

System	*E*	*ZPE*	*TS*	*G*
OH*	-242.57	1.91	7.98	-248.64
O*	-237.85	1.64	7.98	-244.19
OOH*	-247.31	2.00	8.03	-253.34
H_2O	-14.43	0.57	0.68	-14.53
H_2	-6.81	0.27	0.41	-6.95
*	-233.92	1.34	5.54	-238.11
H*	-236.07	1.79	7.83	-242.10

The data in Table S3 is used to draw Figure 5 in the main manuscript and Figure S12 in the Electronic Supplementary Material.

Table S4. The DFT energy E (eV), the zero-point energy correction E_{ZPE} (eV), the entropy contribution TS at 300 K (eV), and the Gibbs free energy G (eV)

System	*E*	*ZPE*	*TS*	*G*
OH*	-243.59	1.96	7.66	-249.29
O*	-238.94	1.70	7.60	-244.84
OOH*	-247.33	2.07	7.63	-252.89
H_2O	-14.42	0.57	0.68	-14.53
H_2	-6.81	0.27	0.41	-6.95
*	-233.92	1.34	5.56	-238.11
H*	-236.07	1.79	7.83	-242.10

The data in Table S4 is used to draw Figure S13 in the Electronic Supplementary Material.

Reference

[1] T. Zhang, Y. Liang, H. Guo, H. Fan, X. Tian, The high piezoelectricity, flexibility and electronic properties of new Janus $ZnXY_2$ (X = Ge, Sn, Si and Y = S, Se, Te) monolayers: A first-principles research, Appl. Surf. Sci. 579 (**2022**) 152017.

[2] L. Hu, X. Huang, D. Wei, Layer-independent and layer-dependent nonlinear optical properties of two-dimensional GaX (X = S, Se, Te) nanosheets, Phys. Chem. Chem. Phys. 19 (**2017**) 11131.

[3] A.K. Singh, K. Mathew, H.L. Zhuang, R.G. Hennig, Computational Screening of 2D Materials for Photocatalysis, J. Phys. Chem. Lett. 6 (**2015**) 1087.

[4] L. Ju, M. Bie, X. Tang, J. Shang, L. Kou, Janus WSSe Monolayer: An Excellent Photocatalyst for Overall Water Splitting, ACS Appl. Mater. Interfaces 12 (**2020**) 29335.

[5] M.S. Hybertsen, S.G. Louie, Electron correlation in semiconductors and insulators: Band gaps and quasiparticle energies, Phys. Rev. B 34 (**1986**) 5390.

[6] S. Albrecht, L. Reining, R. Del Sole, G. Onida, Ab initio calculation of excitonic effects in the optical spectra of semiconductors, Phys. Rev. Lett. 80 (**1998**) 4510.

[7] L.X. Benedict, E.L. Shirley, R.B. Bohn, Optical absorption of insulators and the electron-hole interaction: An ab initio calculation, Phys. Rev. Lett. 80 (**1998**) 4514.

[8] M. Rohlfing, S.G. Louie, Electron-Hole Excitations in Semiconductors and Insulators, Phys. Rev. Lett. 81 (**1998**) 2312.

[9] H. Yang, P. Zhao, Y. Ma, X. Lv, B. Huang, Y. Dai, Janus single-layer group-III monochalcogenides: a promising visible-light photocatalyst, J. Phys. D: Appl. Phys. 52 (**2019**) 455303.

[10] J.K. Nørskov, J. Rossmeisl, A. Logadottir, L. Lindqvist, J.R. Kitchin, T. Bligaard, H. Jonsson, Origin of the overpotential for oxygen reduction at a fuel-cell cathode, J. Phys. Chem. B 108 (**2004**) 17886.